Experimental Investigations Of The Fault Power In A Segmented MHD GeneRator

Author(s): V. J. Hruby and P. Weiss

Session Name: Open Cycle II

SEAM: 19 (1981)

SEAM EDX URL: https://edx.netl.doe.gov/dataset/seam-19

EDX Paper ID: 849

EXPERIMENTAL INVESTIGATIONS OF THE FAULT POWER IN A SEGMENTED MHD GENERATOR*

V. J. Hruby and P. Weiss
Avco Everett Research Laboratory, Inc.
Everett, Massachusetts 02149

Abstract

Experiments have been completed on the AERL MK VII generator to determine the integrity of axial segmentation. The power which may be coupled into an axial fault as well as the response of the interelectrode region to an applied field have been determined. The effects of shorted anodes, open loads, and diagonal connection have also been investigated. Loading faults were found to result in high electrical stresses which caused inter-electrode arcing and anode wall damage.

I. Introduction

The lifetime and performance of the segmented MHD generator is largely dependent on the design of channels to effectively endure high electrical stresses. Breakdown of the Hall field has been widely acknowledged as one of the most serious engineering problems in the development of long duration, combustion driven generators.[1,2] Many experiments have been completed to reveal the mechanisms responsible for the Hall field breakdown,[3] some under actual MHD conditions.[4]

"Fault power" has been defined[5] as the maximum power that a generator may couple into an inter-electrode gap; and is also used to refer to the overall Hall field breakdown problem. The fault power criteria provides a basis for determining electrode pitch and length. Practical considerations, such as water cooling, limit the degree of axial segmentation so it may be necessary to limit fault power in large channels by transversely segmenting electrodes. However, complexity and cost increase with increasing segmentation because the number of power conditioning elements increase and the number of wires inside the magnet increase. In-house studies of magnet warm bore utilization for large channels show that the number of wires and not the coolant manifolding determine the effectiveness of magnet warm bore utilization. It is well known that magnet cost, the largest single item in the MHD topping cycle, goes as the square of its warm bore diameter. Hence, determining fault power, Hall field limitations, and generator behavior under various fault situations is essential for successful channel and control circuitry designs. Five fault power experiments have been performed on the AERL MK VII generator and are discussed in this paper. Most attention was given to the anode because Lorentz forces drive axial arcs into the anode wall whereas axial arcs are pulled away from the cathode wall.

Two of the experiments were concerned with obtaining information to characterize the segmentation design used for MK VII channels. A rheostat was connected between an adjacent pair of electrodes and the maximum, or fault power which could be coupled in the axial direction was determined, under power generating conditions, by varying the rheostat resistance. Also, the response of an adjacent electrode pair to the application of an axial field was determined. This experiment was performed for non-power generating conditions, with and without magnetic field, and examined both diffuse and arcing current transport regimes.

Three experiments addressed the questions of generator behavior, performance, and lifetime under some common fault situations. These were axial shorts on the anode wall of a Faraday loaded channel, opened Faraday loads, and interframe shorts of a diagonally connected generator. All three types of faults resulted in interanode arcing. The arcs were driven into the anode wall by the $\vec{J}x\vec{B}$ force resulting in anode back wall damage. The anode short and diagonal connection experiments were terminated due to anode wall fires. The open Faraday load experiment would have resulted in a forced shutdown had sufficient time been available. The major conclusions of the fault power study are:

1. Initiation of axial breakdown is a function of local thermal conditions and inter-electrode voltage.

2. Local thermal conditions may be strongly influenced by transverse arcing which suggests that transverse current may be an electrical parameter of importance in initiating axial breakdown.

3. Channel electrical connections play a major role in ballasting interelectrode arcs, and hence determine the power dissipated by the arcs.

After a brief description of the experimental facility and hardware the paper discusses each experiment separately including individual summaries, experimental conditions, and results. The final section of the paper is an overview of fault power considerations relevant to the effective design of long duration channels.

II. MK VII Facility Description

The AERL MK VII facility is an open cycle, combustion driven, 20 MW_{th} installation. The ash injected combustor, utilizes #2 fuel oil, air, and oxygen as the reactants. A conventional water cooled copper, iron core magnet is used to provide the induction field of 2.33 Tesla at mid-channel. The magnetic field profile is shown in Fig. 1. The channel is 1m long and rectangular in cross-section having linearly diverging walls with entrance and exit dimensions of 0.07m x .15m and .12m x .18m, respectively. The smaller dimensions pertain to the electrode walls. The channel is followed by a 1m long constant cross-section diffuser. The diffuser is connected to an exhaust tube where the plasma is quenched, scrubbed, and rejected via an exhaust stack.

The channel electrode walls employ 56 water cooled copper electrodes 2.54 cm high and 1.61 cm wide. The electrodes are either nickel plated or capped with protective materials such as stainless steel or inconel. The electrodes are separated by .16 cm wide insulators of either boron

*This research was supported by the U. S. Department of Energy under Contract No. DE-AC010-80-ET15614

nitride or alumina. The channel may be connected in the Faraday or diagonal mode.

Shown in Fig. 2 are the gas side surfaces of the peg type and bar type sidewalls used in the Faraday and diagonally loaded channels, respectively. The cross-section of a typical electrode is also indicated. The profile of resistive loads is indicated in Fig. 1. The peak load is 16.5Ω.

The facility is provided with instrumentation for continuously monitoring pertinent thermal and electrical parameters. Overall burner and channel heat fluxes, as well as individual electrode heat flux, are recorded on strip charts. The laboratory computer, in conjunction with voltage and current transducers, measures and records at 5 sec intervals; interelectrode voltage and load current for each of the 56 electrodes on both the top and bottom walls. In addition, these electrical parameters are displayed on panel meters which may be photographed.

III. Fault Power Coupling Experiments

Summary

The maximum or fault power which may be dissipated between adjacent MK VII electrodes has been quantified. Anodes and cathodes were investigated for both clean and slagging wall conditions. The fault power was determined by connecting a rheostat to adjacent electrodes and mapping out the voltage-current characteristic of the electrode pair, under power generating conditions, by varying the rheostat resistance. The voltage-current characteristic was nearly linear. The fault power was determined by finding the maximum of the voltage-current product. For anodes 29-30 under slagging wall conditions at a 60 kW average power generating level, the fault power occurred for a 5Ω rheostat resistance and was 100 watts. The core flow mid-channel conditions at 60 kW power level are J_y = 0.8 A/cm^2, E_y = 1.2 kV/m, and E_x = 1.1 kV/m.

Since the voltage-current characteristics were approximately linear, it was decided to determine the fault power on the anode wall, as a function of number of shorted anodes, by measuring the open circuit voltage and short circuit current only. It was found that for slagging wall conditions at a 60 kW power operating level that 0.9 kW could be dissipated between anodes 27-28 when anodes 28 through 35 are shorted. The fault power varies almost linearly with number of shorted anode electrodes.

Experimental Systems, Procedures, and Operating Conditions

Figure 3 shows a schematic of the interelectrode rheostat connection. Rheostat current and interelectrode voltage were monitored with transducers. The output of the transducers were recorded on a strip chart and X-Y plotter. To obtain V-I characteristics for experiments where electrodes were shorted, interelectrode shorting switches were connected between electrodes 28 through 36. Interelectrode voltage and short circuit current signals were digitized and recorded with the aid of the laboratory data acquisition system.

Experiments using the rheostat system proceeded by adjusting the rheostat resistance in discrete increments and allowing steady conditions to be established. The anode electrode shorting test was performed by sequentially closing the shorting switches in the downstream direction starting with electrodes 28-29. Personnel safety required shutdown of the magnet before each shorting switch was closed. After each switch was closed the magnet power was restored and a few minutes elapsed for steady operation.

Table 1 lists the operating conditions investigated. Experiments with the rheostat were done for both the clean and slagging wall conditions. The shorting experiment was done for the slagging wall condition only. The electrodes investigated for clean wall conditions were anodes and cathodes 27-28. For slagging wall runs electrodes 29-30 and 31-32 on the anode and 27-28 on the cathode were tested.

Experimental Results

Figure 4 is a typical voltage-current characteristic for the anode gap 31-32 under slagging wall power generating conditions; as drawn real time by the X-Y plotter. Several runs with rheostat resistance varying from 200Ω to 0.7Ω are seen to have been completed. During the course of the test the open circuit interelectrode voltage was seen to have varied from 36 to 50V. The short circuit current was about 9.5A. The rheostat resistance was regulated to values which are indicated by the radial lines. Fluctuations in the generator electrical parameters caused the radial line tracing at each discrete rheostat resistance.

Figure 5 shows the voltage-current characteristics constructed from average data for electrodes 27-28 on the anode and cathode for clean wall conditions, and anodes 29-30 and cathodes 27-28 for slagging wall conditions. The plots all exhibit a slight curvature. Generally, the electrodes which have large interelectrode voltages have large short circuit currents. Also shown in the figure are lines of constant power. The constant power line tangent to the voltage-current characteristic is the fault power. For anode electrode pair 29-30 under slagging wall conditions the fault power is seen to be approximately 100 watts. Clean walls have considerably lower fault power which is consistent with the lower generated power levels resulting from higher combustor and channel wall heat loss. The voltage-current characteristic of cathodes 27-28 under slagging conditions is of particular interest as the open circuit voltage is inconsistently high. This result is due to the behavior of the cathode nonuniformities[6] typical of slagging wall channels. The low short circuit current is incongruous with the high open circuit voltage and is probably the result of a shift in the cathode nonuniformities during the run.

Figure 6 shows the results of the shorting experiment. Eight linear voltage-current characteristics were constructed from the data obtained by successively shorting anode electrodes. The fault power would be the product of half the open circuit voltage and half the short circuit current. The fault power is plotted in Fig. 7, as a function of the number of downstream anode electrodes shorted and is seen to increase almost linearly with the number of shorts at the rate of 140 watts/short. With seven anode electrodes shorted the fault power is approximately 0.9 kW.

Fault power may be defined in terms of generator electrical and geometric parameters as follows:

$$P_{fault} = C\, V_{o.c.}\, I_{s.c.} \quad (1)$$

where

C	Constant
$V_{o.c.}$	interelectrode open circuit voltage
$I_{s.c.}$	interelectrode short circuit current

with

$$V_{o.c.} = E_x P \quad (2)$$

and if it is assumed that the short circuit equals the Faraday current, then

$$I_{s.c.} = J_y P \ell \quad (3)$$

where

E_x	free stream axial field
J_y	current density
P	electrode pitch
ℓ	electrode length.

Inserting equations (2) and (3) into equation (1) yields

$$P_{fault} = C\, E_x J_y P^2 \ell \quad (4)$$

For a Faraday loaded generator, the fault power would correspond to the product of half the open circuit voltage and short circuit current, therefore, C=0.25 in equation (4). For a diagonally connected generator C=0.5 since the current which may be coupled into a fault is from an area of 2P. Using typical values for E_x, P, and ℓ in equation (4), $P_{fault} \approx 60$ watts for a Faraday loaded machine. This agrees reasonably well with the experimentally determined value of 100 watts and is probably lower due to the linear voltage-current characteristic approximation.

It should be noted that the fault power and the power in a fault causing destruction of channel elements are in general two different quantities. The former, as shown in Eq. (1), may be defined using free stream electrical parameters and electrode size. The latter depends on the electrode wall design only. However, for viable channel designs, the fault power should be equal or by some margin of safety smaller than the power that causes channel destruction.

Conclusions

1. The fault power for slagging wall operation of the MK VII on the anode wall is 100 watts and increases linearly with the number of shorted anode electrodes.

2. The voltage-current characteristic of an electrode pair under power generating conditions has a slight curvature and is well approximated by a straight line.

IV. Applied Field Experiments

Summary

The response of the MK VII channel wall interelectrode region to the application of an axial field has been determined. A DC power source was used to apply a voltage to an adjacent pair of anode electrodes. Various electrode and insulator materials were investigated over a range of flow conditions for both clean and slagging walls. Some experiments were performed in the presence of a magnetic field but without seed to avoid induced EMF. Below a threshold voltage, 60-100V, the electrode pair voltage-current characteristic was somewhat linear indicating an electrode pair resistance of 70-270Ω for clean walls and 35-270Ω for slagging walls. Slag layer leakage accounted for the lower slagged wall resistance. New unslagged electrode walls have interelectrode impedance of 300Ω and greater. For voltages exceeding the threshold level an abrupt decline in electrode pair resistance to 2-4Ω occurred. This behavior was due to a change in the current transport mode from diffused to arcing. Tests performed in a .5-2 Tesla magnetic field resulted in interelectrode insulator arc damage caused by interelectrode arcs driven by $\vec{J}\times\vec{B}$ forces. The time for an interelectrode arc to penetrate the full height of an insulator ranged from 4 - 11 sec and was found to be a function of insulator material and the $\vec{J}\times\vec{B}$ force.

Experimental Systems, Procedures, and Operating Conditions

A schematic of the experimental circuitry is shown in Fig. 8. A regulatable DC power supply was connected in series with a ballast resistor, 3.8 or 8.5Ω, and any adjacent anode electrode pair. For tests performed without magnetic field a 300V, 35a power supply was used and for test conditions with magnetic field a 500V, 200a power supply was used. Transducers were used to monitor current, interelectrode voltage, and power supply voltage. A multichannel strip chart was used to record the electrical parameters. Also, an X-Y plotter was employed to directly obtain the voltage-current characteristic of an electrode pair. Figure 8 shows the arc luminosity system that was used to detect an interelectrode arc after it penetrated the full height of an insulator under the action of $\vec{J}\times\vec{B}$ forces. Slots were milled in the anode wall backboard under the insulators separating electrode pairs 15-16, 33-34, and 43-44. These slots were viewed with fiber optic tubes. The free end of the fiber optic tube was connected to a photocell. The photocell output was amplified and recorded on the strip chart along with the electrical parameters.

For tests performed without magnetic field, the voltage-current characteristics were obtained by regulating the power supply in discrete voltage increments starting at zero voltage and terminating at the arcing threshold voltage level. In order to insure that a steady response to each voltage level was achieved, 3-5 mins. were permitted to elapse before the power supply voltage was incremented. The tests run with magnetic field proceeded by regulating the power supply to some voltage above the threshold level and shutting down the power supply when a burst of luminosity was registered by the strip chart recorder. The time elapsed between the abrupt decline of interelectrode voltage and the detection of luminosity at the backboard would be indicative of insulator cutting time.

The operating conditions investigated are listed in Table 2. Static conditions (i.e., no flow) were checked first. Next, tests were conducted in flowing air only followed by tests with unseeded combustion products and clean walls. The magnet was turned on and the three electrode pairs

instrumented for arc luminosity detection were tested. Finally, the effects of seeding were explored and experiments were completed with slagging walls.

Experimental Results

Table 3 is a listing of the electrode pairs tested, the electrode materials, and the channel operating conditions. The electrode materials evaluated were copper, nickel plated copper, tungsten/copper, steel, stainless steel, and molybdenum. All interelectrode insulators were boron nitride except for the insulators used with electrode pairs 33-34 and 43-44 which were alumina.

A typical experimental result for a run performed in the absence of a magnetic field is shown in Fig. 9 which is the voltage-current characteristic, as recorded by the X-Y plotter, of electrode pair 52-53 with slagging walls. The electrode pair may be seen to have been subjected to four voltage levels, namely, 49, 54, 63 and 71V. The slope of the voltage-current characteristic changed from 160Ω for voltages lower than 49V, to 70Ω for voltages exceeding 49V. This change in slope did not occur for the clean wall runs. In addition, strip chart recordings indicate that the slope change occurred only after time intervals of a few seconds. The increasing slag conductivity (decreasing dV/dI) is caused by slag polarization due to interelectrode charge transport and by local Joule dissipation heating the slag to the threshold of electrothermal instability. Passing the critical point of this instability results in a breakdown with corresponding arcing. Arcing initially occurred at 63V and was indicated by an abrupt drop in voltage to 33V and an increase in current from 1.5 to 8.4 amps. The arc was immediately extinguished and prearcing conditions were restored. This behavior is best illustrated by Fig. 10 which shows the portion of the strip chart recording just after the voltage was regulated to 63V. After a delay of 53 sec, the interelectrode voltage dropped and was accompanied by an increase in current. This condition lasted for a brief period of time and prearcing conditions were restored. After a delay of 18 sec, the arcing, arc-extinguishing process resumed. This behavior may be explained as follows. After the electrode pair threshold voltage is exceeded interelectrode arcing results. The net effect on the applied field circuit is a change in electrode pair resistance from, in this case, 40Ω to 4Ω. As this change occurs the power supply voltage remains constant and the current in the circuit increases since the equivalent circuit resistance has dropped. The larger current results in a greater voltage drop across the ballast resistor and the voltage across the electrode pair must therefore decline. As mentioned above, the post-arcing interelectrode voltage drops to 33V which is insufficient to sustain the arc. The arc extinguishes and prearcing conditions are restored followed by re-arcing.

Figure 11 is a plot showing the threshold and arcing voltage-current positions for all electrode pairs tested without magnetic field. For static, air flow, and unseeded combustion conditions, threshold voltages were in the range 250-300V. At these conditions the arc voltage drops were approximately 35V for currents of approximately 25 amps. For clean and slagging wall plasma conditions threshold voltages ranged from 60-110V. Arc voltage drops were 30-45 volts at 5-15 amps. There were no noticeable variations in the voltage-current characteristics with channel wall location or electrode material. The only slag effect was that of polarization and served to increase the prearcing leakage current but did not effect the threshold voltage value.

Also shown in Fig. 11 is the applied field data of Curtis, et al.[7] Their experiments were performed with Al_2O_3 insulators of the same thickness and length with clean wall conditions. Excellent agreement of threshold voltages and the prearcing electrode pair resistance, may be observed.

Figure 12 shows a typical strip chart recording for a run performed with magnetic field but without seed. The strip chart recording shows the interelectrode voltage, current, and luminosity detection system traces for anode electrodes 43-44 under clean wall conditions. Arcing occurred at an average voltage of 100V. The arc voltage drop and current are seen to be approximately 45V and 15a, respectively. A pulse in the luminosity trace indicates the arrival of an interelectrode arc at the anode wall backboard. The strip chart indicates an insulator cutting time of 4.5 sec, since that was the duration of time between the drop in interelectrode voltage and the detection of luminosity at the backboard.

Figure 13 is a post-test photograph showing electrode pair 33-34, the Al_2O_3 insulator separating the electrodes, and the anode wall backboard. The arc track across the insulator is seen as well as the point where the arc was extinguished by the backboard. The photograph also shows the slot that was milled in the backboard under the insulator and the clips which held the fiber optic tubes.

Figure 14 is a plot of the product of magnetic field strength and arc current versus insulator cutting time for the three electrode pairs tested. The plot indicates that for Al_2O_3 insulators a 40% reduction in the magnetic field strength-current product results in a 60% increase in insulator cutting time. The plot also demonstrates that boron nitride insulators are penetrated by arcs approximately 60% faster than alumina insulators under the same condition.

Conclusions

1. For applied field conditions, threshold voltage levels for MK VII electrode pairs ranged from 60-100V.

2. Prearcing electrode pair resistance was 90-270Ω for clean walls and 35-275Ω for slagging walls. Slag layer polarization and heating by Joule dissipation accounted for the lower resistance.

3. There were no noticeable effects on the threshold voltage level with slag, electrode material, or channel location.

4. Arcing occurred at the threshold voltage in some cases immediately, and in other cases after delays ranging from 1/2 sec to 2 1/2 min.

5. The response of an electrode pair to an applied voltage is a strong function of the circuitry employed (i.e., power supply

characteristics and ballast resistance values).

6. Anode interelectrode arcs, in the presence of a magnetic field, are driven into the electrode wall and cut through boron nitride or alumina insulators.

7. The time for a stable arc to cut through an Al_2O_3 insulator is inversely related to the magnetic field strength-current product. Boron nitride insulators appear to be less resistant to arc penetration than alumina insulators. For the conditions of the experiment the time to cut an insulator is of the order of 5 seconds.

V. Shorted Anode Experiment

Summary

The MK VII generator behavior with externally shorted anodes has been determined.[8] Nine anode electrodes were sequentially shorted in the downstream direction starting with electrode pair 28-29. This was accomplished by external short circuit switches fitted with instrumentation for measuring the short circuit current. An arc luminosity system similar to that described in Section IV, was used to monitor the gaps between anodes 25-26, 26-27, and 27-28.

The gap voltage 27-28, anode 28 transverse plasma current, and the external short circuit currents increased monotonically with number of shorted anodes. The load currents associated with shorted electrodes were inversely related to the short circuit currents. With anodes 28 through 35 externally shorted, the voltage between anodes 27 and 28 was 95V and the transverse plasma current associated with anode 28 was 52 amperes. At this condition the strip chart recorder channel indicating 27-28 interanode voltage showed signs of arcing. Interelectrode arcing was characterized by instantaneous drops in voltage. With nine electrodes externally shorted the frequency of arcing and arc extinguishing, for electrode pair 27-28, increased. After approximately 64 min. at this condition, electrode pair 27-28 became internally shorted due to arc damage. The high electrical stresses shifted upstream to anode pair 26-27 causing similar arcing behavior and subsequent electrode shorting. The self-propagating lectrode shorting continued in the upstream direction until the test was terminated by an emergency shutdown due to a burning anode wall. Post-test examination of the channel wall components revealed many arc damaged interanode insulators and extensive charring of the fiberglass anode wall backboard. The backboard became charred, and hence, electrically conductive by assault from interelectrode arcs driven by $\vec{J}x\vec{B}$ forces. The damaged backboard, and tie rods compressively loading groups of electrodes, provided the permanent internal shorting current path.

Experimental Systems, Procedures, and Operating Conditions

Figure 15 is a schematic of the MK VII electrical connections and instrumentation used for the test. In addition to the standard facility instrumentation, eight external short circuit connections equipped with shorting switches, ammeters, and current transducers were installed between anode electrodes 28 through 36. The shorting connection and instrumentation are indicated by the dashed line in Fig. 15. The interelectrode voltage for anodes 25-26, 26-27 and 27-28 were monitored by a strip chart recorder. Slots were milled in the anode wall backboard under the insulators associated with anode pairs 25-26, 26-27 and 27-28. The slots were used to accommodate the arc luminosity detection system described in Section IV.

Once stable, generator operation at specified conditions was achieved, external shorting of anodes began. Personnel safety made it necessary to turn off the magnet before each shorting switch was closed. Electrode pairs were shorted one at a time in the downstream direction starting with anodes 28-29 and ending with 35-36. After each shorting switch was closed, the generator was allowed to run for approximately five minutes during which time the instrumentation was consulted for indications of electrical fault development. Table 1 lists the operating conditions, which are typical for slagging wall operation of the MK VII.

Experimental Results

Figures 16a through 16c illustrate the generator electrical behavior at 3 representative times during the experiment. The distribution of interelectrode voltages, total potential, load currents, and interanode short circuit currents are shown in each figure. Figure 16a represents the initial fault free state of the generator. Some cathode nonuniformities are present creating a step like Hall voltage distribution. Peak load currents correspond to an approximately .85 A/cm^2 current density. After 9 anodes were externally shorted, just prior to fault damage, the voltages and currents were distributed as shown in Fig. 16b. This figure illustrates the conditions which lead to fault propagation in the upstream direction. The interelectrode voltage is seen to be larger on the upstream end of the shorted group than the downstream end. This coupled with the concentration of plasma current on the upstream electrode of the shorted group results in high electrical stresses which shift to successive upstream electrodes as internal electrode shorts occur. Figure 16c shows the voltages and currents just prior to the test termination. The section from station 28 to 13 is internally shorted via the charred anode backboard. This condition eventually resulted in a forced shutdown.

The local voltage and current evolution at the upstream end of the shorted group is shown in Figs. 17 and 18, respectively. Figure 17 shows the voltage between anodes 27-28 as a function of the number of shorting switches closed. The plot demonstrates the almost linear increase in interelectrode voltage from 15V under normal operating conditions to 95V when nine anodes are shorted downstream. Figure 18 shows plots of the short circuits, load, and transverse plasma currents as a function of the number of shorting switches closed. As successive downstream anodes are shorted, the short circuit current between electrodes 28 and 29 is seen to increase from 0A with no electrodes shorted to 46A with electrodes 28 through 36 shorted. As the electrode pair 28-29 short circuit current increases, Fig. 18 demonstrates that electrode 28 load current decreases from 12 amperes when there is no short circuit current to 8 amperes when the short circuit

current is 44 amperes. Figure 18 shows the current leaving anode 28 and entering the plasma. This current is the sum of the load current and short circuit current. The figure shows that the anode electrode 28 transverse plasma current increases from 12A under normal conditions to 52A when electrodes 28 through 36 are shorted.

The first indication of interelectrode arcing occurred with eight electrodes shorted. This condition is shown in Fig. 19 which is the strip chart recording during that time period. Interelectrode voltage for gap 27-28 shows an arcing potential of 95V. Interelectrode arcing was characterized by an instantaneous voltage drop between anodes 27-28 accompanied by an instantaneous voltage increase between anodes 26-27. Restoration to prearcing voltage levels occurred immediately afterward indicating that the arc was extinguished after a short delay. This behavior resulted because the generator could not sustain a high enough interelectrode voltage, in the presence of the large arcing current, to support a stable arc. This is similar to the situation described in Section IV.

After anodes 28 through 36 were externally shorted, arcing between electrodes 27 and 28 continued for approximately 64 min with increasing frequency until the neighboring anodes became permanently shorted due to arc damage. The arc luminosity detection system registered high luminosity during the period when the adjacent electrode became permanently shorted but was not useful for determining insulator arc cutting times as the interelectrode arcs were not stable and the insulator damage resulted from many short duration arcs. The internal shorting of anode pair 27-28 resulted in a shift of electrical stresses (i.e., interelectrode voltage and transverse plasma current) to anode pair 26-27. This gap began arcing and permanently shorted after 20 minutes. The axial fault continued self-propagating in the upstream direction, in a similar manner, consuming electrodes 27 through 23. Table 4 lists the electrical parameters, magnetic field strength, electrode pair shorting time, and insulator/backboard condition for those electrodes incorporated into the fault. The arcing potential and plasma currents at arcing conditions are seen to range from 85-105V and 24-62A, respectively. Post test examination of the anode wall components revealed arc damaged insulators and charred backboard for all electrode pairs except 25-26. This insulator was not arc damaged which is consistent with the strip chart recording which showed no signs of interelectrode arcing before shorting. Electrode shorting in this case was the result of backboard failure due to overheating and subsequent charring. The internal shorting of electrode pair 23-24 was followed by the simulatneous shorting of electrodes 13 through 23. This event caused a forced shutdown of the generator due to a burning anode wall backboard.

Figure 20 shows post-test photographs of the anode wall with electrodes 1 through 33 removed. The charred backboard region, which provided the electrode shorting path, is seen to extend from electrode 13 to 20. The backboard slots to accommodate the arc luminosity detection system may also be seen. The figure also shows the upstream side of anode 27. The electrode and insulator arc damage is evident indicating a multitude of interelectrode arcs. Also shown are the holes accommodating the tie rods which compressively load groups of electrodes.

In order to compute the plasma currents listed in Table 4, the load and short circuit currents associated with the electrode must be added, as described previously. For electrodes which shorted due to internal faults the short circuit currents were unknown as they could not be measured. In order to estimate this short circuit current, and hence facilitate the computation of the transverse plasma current, a relationship between the load current and short circuit current was sought. Figure 18 demonstrates the relationship between the load current and short circuit from data obtained with the externally shorted electrodes. If load current is plotted against short circuit, it is found that the ratio of the change in short circuit current to the change in load current is approximately ten. This relationship was used to estimate the electrode fault short circuit currents from the measured load currents. This provided the basis for the estimate of the transverse plasma currents reported in Table 5.

The overall effect of the axial fault on the generator performance is summarized in Table 5. The data indicates that the shorting of electrodes 13 through 36 resulted in a 10% decline in Hall voltage and a 20% drop in the power generating level.

Conclusions

1. At representative slagging wall, Faraday loaded MK VII conditions, an interanode voltage of 80-100V and a transverse plasma current of 45-60A, on the downstream electrode, are required to initiate interelectrode arcing.

2. The Hall field breakdown on the anode wall may propagate in the upstream direction, with each shorted electrode pair creating the electrical conditions for interelectrode arcing with upstream electrodes.

3. The axial internal faults were caused by arc damage, and subsequent charring of the NEMA Grade G-10 fiberglass material used for the backboard and electrode tie rods. Replacing the resin rich G-10 fiberglass with G-7 fiberglass may prevent charring and the corresponding loss of dielectric properties of the back wall.

VI. Open Faraday Load Experiment

Summary

The MK VII generator behavior under slagging wall conditions with six Faraday loads removed in the mid-channel section (24 through 29) has been determined. As an increasing number of loads were opened the anode interelectrode voltage on the downstream end of the open group increased monotonically from 30V in the fully loaded condition, to 90V with five loads open. On the upstream end of the open group the polarity reversed and was -75V with five loads open. The cathode gaps within and at the end of the unloaded group supported little or no voltage gradient. The gap at the upstream end carried nearly all the Hall voltage. This is attributed to cathode slag leakage. The data indicated some redistribution of current generated in the unloaded section.

The current to the two or three electrodes just upstream and downstream of the open group increased such that the overall generated power decreased only slightly.

Strip chart recordings indicated interelectrode arcing between anode electrodes 29 and 30. The duration of the test was 4 hours and 15 minutes and no emergency shutdown due to interelectrode arc damage was required. Post-test examination of the channel components revealed arc tracks in the insulators separating anodes 28, 29 and 30. None of the arc tracks reached the electrode tie rods or penetrated the full height of the insulators. However, it is believed that eventual damage to the anode back wall would have resulted.

Experimental Systems, Procedures, and Operating Conditions

The instrumentation employed for this experiment was the standard facility data logging system. In addition strip chart recorders were used to monitor the interelectrode voltage for anode and cathode electrodes 23 through 32.

The experiment proceeded by allowing the generator to achieve steady operation at specified conditions and opening loads one at a time. Figure 21 is a plot of generated power vs time. It shows that after a brief debugging period loads were opened one at a time in the order 28, 27, 29, 26, 25 and 24. Due to design constraints the magnet was shut down before removing each load. After the magnet power was restored Fig. 21 shows operation at each condition varying from 10 min to 1 1/2 hours. With loads 25 through 29 removed the nitrogen/oxygen ratio was lowered from 0.8 to 0.7 resulting in an increase in average generated power from 50 kW to 75 kW. The test was terminated due to run time considerations rather than channel failure. Operating conditions are listed in Table 1 and are typical for MK VII slagging wall conditions.

Experimental Results

The distribution of interelectrode voltages, Hall voltage and current just prior to test termination is shown in Fig. 22. The initial fault free distributions was essentially the same as shown in Fig. 16a. Observing Fig. 22, one notes several substantial differences between the anode and cathode behavior. All these differences can be attributed to the slag leakage on the cathode wall. Most notable is the absence of appreciable negative intercathode voltages that are expected to appear in the downstream portion of the unloaded group, and the very high (130V) yet harmless intercathode voltage at the upstream end of the unloaded group.

As shown, the maximum Faraday voltage reached is about 490V. The theoretical UBh (h is the local generator height) is about 500V. Hence, reloading a group of electrodes over a region that corresponds to 60% of generator height allows the generator to change its external load factor, k, from k=0.5 to 1. This of course depends on the number of insulators involved and their ability to carry voltage.

Figure 23 is a plot of interanode voltage as a function of number of open loads for the adjacent anodes just upstream and downstream of the open group. The anodes involved are identified for each point in the figure. The downstream interanode voltage is seen to increase from 30V with no open loads to 95V with loads 25 through 29 removed. The upstream anode interelectrode pair exhibits an interelectrode voltage polarity reversal of -75V when loads 25 through 29 are removed. The upstream and downstream interanode voltages increase somewhat symmetrically about the nominal value for a fully loaded condition.

Figure 24 is a plot showing the spatial distribution of currents for electrodes 20 through 35. Average current conditions at each loading condition are shown. This plot illustrates that current redistributes such that nearly all the power in the unloaded section is dissipated in the loads adjacent to the open group. For example, with load 28 open, there is an increase of 3 amps to load 29. With load 27 and 28 open the current to load 26 and 29 increases by 1 amp and 3.5 amps, respectively. There are some anomalies attributable to shifting cathode nonuniformities.

Figure 25 is a portion of the strip chart recording with electrodes 25 through 29 open. It shows interanode voltages 29-30, 30-31, and 31-32 and intercathode voltages 23-24 and 24-25. The intercathode 24-25 voltage is seen to abruptly shift from 16V to approximately 0V. This is an example of the dynamic nature of cathode nonuniformities. The strip chart also indicates that at this condition arcing between anode electrodes 29 and 30 first began. The arcing is characterized by the large amplitude changes in voltage. The arcing voltage level appears to be approximately 120V.

Figure 26 is a post-test photograph of the upstream side of anode 29. The interelectrode insulator is heavily arc damaged which supports evidence of interelectrode arcing indicated by the strip chart. None of the arc tracks penetrated the full height of the insulator or reached a tie rod. This explains why the backboard was undamaged and no electrode shorting occurred. Also, a small arc track was found in the insulator separating anode electrodes 28 and 29.

No arc tracks were found in the upstream portion of the unloaded group. This is expected because that region had negative interanode voltages. The cathode wall was undamaged despite very high voltages (see Fig. 22). This is because of the favorable Lorentz force direction acting on cathode axial arcs.

Conclusions

1. Removing five loads from the mid-section of the MK VII generator results in a current redistribution which maintains approximately the same generated power.

2. The Faraday voltage in the unloaded section reached approximately UBh (k=1).

3. The cathode interelectrode voltages differ dramatically from that of the anode. High cathode slag conductivity and leakage causes these differences.

4. Interelectrode arcs resulting from an open load fault appear to dissipate less power than interelectrode arcs caused by shorted anodes. This conclusion is arrived at on the basis of experiments run under the same generator conditions. Shorted anodes resulted in an arc damaged backboard after

1 hour, whereas opening loads resulted in minimal insulator damage after 4 hours.

VII. Diagonal Connection

Summary

The behavior of the diagonally connected MK VII generator with interframe shorts has been investigated.[9] The interframe shorts were not externally imposed but were internally generated by cathode nonuniformities[6] shorting groups of cathodes. These nonuniformities were projected through the diagonal links onto the anode wall where destructive faults occurred. Data were collected for various loadings and over a range of flow and slagging conditions. Continuous frame construction was achieved using sidewalls of diagonally arranged bars externally wired to anode and cathode electrodes. Load voltage and current, as well as interframe voltages and total frame currents, were continuously monitored. Two frames were completely instrumented to measure individual electrode and bar currents.

At standard MK VII conditions, using Eastern ash as the slagging medium, 45 kW was indicated as the maximum generated power at a load of 10Ω-12Ω. Using Western ash as the slagging medium decreased the generated power by 15% and decreasing the nitrogen/oxygen ratio from 0.8 to 0.6 increased the generated power by 50%. In general, the overall electrical parameters (i.e., load voltage and current) were quasi-steady but the interframe voltages and total frame currents were unsteady with frequent polarity reversals. It was also found that the sidewall bars adjacent to anode and cathode electrodes act as electrodes but do not necessarily exchange current in the same direction as the adjacent electrodes.

After 7 hours and 20 minutes of power generation the test was terminated due to burning of the anode back wall. Post-test inspection of the channel revealed extensive damage to the anode wall backboard and electrode tie rods. In addition, many of the interanode insulators were cut by interelectrode arcs driven by $\vec{J}x\vec{B}$ forces.

In general, the electrical stresses that initiated the destructive faults were lower than those measured in the Faraday channel experiments. As shown by Eq. (4), the fault power for the same electrode pitch and same free stream conditions may be higher in the diagonal than in the Faraday channel.

Channel Connections, Procedures, and Operating Conditions

To provide the continuous frame construction used in the diagonal connection, the anode, cathode, and sidewalls were wired as shown in Fig. 27. The gas side surface of a 3-piece diagonal link is shown in Fig. 2. The diagonal bar segments and the anode and cathode electrodes were connected with external wires to provide an uninterrupted current path. All 47 frames, with the exception of frames 26 and 32, were provided with an external current path equipped with a current transducer for monitoring the total frame current. Frames 26 and 32 were wired such that the current entering or leaving each electrode and bar could be monitored. This configuration is also shown in Fig. 27. The bar and electrode currents for frames 26 and 32 were displayed on panel meters.

The channel loading is shown in Fig. 27. The first nine electrodes on the anode wall and the last nine on the cathode wall were the power take-off section. Each of the power take-off electrode connections was ballasted with a 1Ω resistor. Diodes were wired in series with the ballasts to prevent current circulation.

The experiment was run on two consecutive days. A large portion of the experiment was devoted to developing a load line. Ample time was allowed to achieve stable operation after each change in operating conditions. The sequence of events are shown in Fig. 28 which are plots of total generated power as a function of burner time for each day.

Table 6 lists the operating conditions investigated during the experiment. Five operating conditions were run. The fixed parameters were mass flow, combustor pressure, potassium concentration, slag carryover, inlet Mach number, and magnetic field. The nitrogen/oxygen ratio, ash type, and generator load were varied. Table 7 lists the constituents of the Eastern and Western ash used for the slagging medium.

Experimental Results

Figure 29 shows the load line that was developed for the generator from the data obtained at the various operating conditions. Three data points were obtained at a single flow condition and a load line was constructed. For Eastern ash at N/O = 0.8, a maximum power of 45 kW is indicated for a 10-12Ω load. Use of Western ash as a slagging medium is seen to decrease the generated power. The mean and RMS cathode interelectrode voltages for electrodes 12 through 44 are plotted against time in Fig. 30, for both Eastern and Western ash. Comparison of the two plots shows that Western Ash has a higher RMS voltage than Eastern ash. The RMS voltage is approximately equal to the mean voltage in the case of the Eastern ash whereas for Western ash the RMS voltage exceeds the mean, indicating fluctuations greater than 100%. This indicates greater severity of cathode nonuniformities with Western slag than with Eastern slag. Note that the mean voltages for Eastern and Western ash are nearly identical.

Figure 31 summarizes some of the information obtained from frames 26 and 32 which were completely instrumented with ammeters. As mentioned previously the currents flowing through each electrode and bar split were measured. Ammeters were mounted on a panel and photographed every fifteen minutes. The meter readings are indicated by the numbers 1 through 8 in Fig. 31. Values of these readings are listed for various operating conditions and times. The currents entering or leaving the side wall bars and electrodes have been computed from the ammeter readings and are labeled "a" through "h" in the figure. The major conclusions are: a) sidewall bars adjacent to anodes and cathodes act as electrodes but do not necessarily exchange currents in the same direction as the adjacent electrodes, and (b) the middle section of the three section bar wall does not draw current from the plasma. The practical implications of these conclusions are: a) electrically continuous bars must be capped with protective materials to achieve acceptable lifetime, and b) selection of protective cap materials is complicated by the bi-direction-

ality of the collected current, requiring the protective cap to perform satisfactorily as both anode and cathode. Although these conclusions are not directly connected to fault power considerations, they are certainly noteworthy.

To illustrate the behavior of the anode wall interelectrode voltage and the frame currents, a plot of gap voltage 29-30 is shown in Fig. 32 and the total frame current for frame 29 is shown in Fig. 33. The operating conditions which correspond to each power generating interval may be determined from Fig. 28.

Figure 32 shows the highly unsteady behavior of the interframe voltage for both days of running. During the first day at a burner time of approximately 325 minutes the voltage dropped from an average level of approximately 60 volts to an average level of about 12 volts. This drop may be the result of interelectrode arc damage, or of cathode nonuniformities shifting the high voltage away from cathode gap 20-21. During the second day the voltage level increased dramatically when the N/O ratio was reduced to increase the power generated from 36 kW to 70 kW. Note that the RMS and mean cathode voltages shown in Fig. 30 are in fact interframe voltages that represent interanode fluctuations as well.

Figure 33 shows the total frame current for electrode 29 for both days. The current is unsteady with frequent reversals of direction. This is another example of local current bi-directionality making an anodic part of the frame cathodic and vice versa. An observation which may be made is that the current is somewhat constant and unidirectional when the voltage between electrodes 29 and 30 is below approximately 35 volts. For voltage levels exceeding this value, the current is quite unsteady with frequent current flow direction reversals. This observation was not true in all cases.

As previously mentioned, the test was terminated due to a burning anode wall. Post-test examination of the anode wall revealed that the backboard was severely burned under electrodes 32 through 37. The tie rods which compressively loaded these electrodes were also burned. Figure 34 shows the conditions of the anode wall. Electrodes 13 through 45 have been removed to reveal the charred backboard. Resistance measurements indicate the charred region to have a very low impedance. The backboard appears to have provided an axial current path between electrodes 21 through 37. Another axial current path was provided by the charred tie rods, not shown. Both the tie rods and backboard were made of fiberglass NEMA Grade G-10. The cathode wall and sidewalls of the channel were undamaged. Figure 35 is a post-test photograph of the upstream side of anode electrode 32. Multiple arc tracks may be seen in the interelectrode insulator. This was typical of the condition of all the insulators separating anode electrodes 26 through 34. Some arc tracks extended the full height of the insulator and others terminated at the tie rods. This evidence explains how the tie rods were burned and how the backboard burning was initiated.

Conclusions

1. The interframe voltages and frame currents of a diagonally connected MHD generator are unsteady, but the total load current and load voltage is quasi-steady.

2. Although the exact sequence of events is not known, the channel tested appears to have failed due to a damaged fiber resin backboard and electrode tie rods. The backboard and tie rods became charred, and hence electrically conductive, by interelectrode arcs which penetrated the insulators separating electrodes.

3. At constant flow conditions and slagging rates, the use of Western ash as the slagging medium results in about 15% reduction in generated power compared to Eastern ash as the slagging medium. This behavior is attributed to the greater degree of polarization of the Western ash which increases leakage currents on the cathode wall. This is demonstrated by increased cathode RMS voltage.

4. The bar type sidewalls act, in some cases, as electrodes exchanging current with the plasma. The direction of the current flow may be the same as neighboring anodes or cathodes, or it may be opposite to the adjacent electrodes resulting in a current circulation at the corners of the channel. Choosing a protective cap material for bars which draw current is complicated by the existence of current reversals which make cathodic bars anodic and vice versa.

5. Interanode arcing which eventually resulted in a forced shutdown occurred at lower measured interanode voltages than those measured in the anode short experiment with a Faraday channel. The Faraday load acts as a local ballast which is absent in diagonally connected generators with only global ballast. Lack of local ballast in the diagonal channel allows interelectrode arcs to be sustained for relatively long durations resulting in arc power dissipation which is much higher than in Faraday channels.

VIII. Overview

The AERL fault power program revealed the character and behavior of the MK VII generator with respect to axial insufficiencies. The experiments determined; (1) the generator fault power as a function of shorted anodes, (2) the electrothermal stress levels required to initiate breakdown, (3) the generator behavior for various loading and fault conditions, and (4) generator design deficiencies in connection with axial breakdown.

In general, axial breakdown phenomena may be described as follows. Internal fault initiation depends on local electrothermal stresses. Fault damage to the channel depends on global channel conditions such as type of loading (Faraday/diagonal), type of fault (open Faraday load, axial anode short, interframe short) and the precise electrode/insulator back wall design. The loading and type of fault determine the stability of the breakdown via ballasting of the fault current, and therefore determine the average power dissipated by the interelectrode arc.

The order of fault severity, beginning with the most serious, is (1) interframe short(s) in diagonally connected generator, (2) interanode short(s) in a Faraday generator, and (3) opened Faraday loads. The ranking reflects the strong

dependence of the fault average power on the ballasting of the fault current.

The following conclusions have been reached as a result of the fault power experiments.

1. There are two distinct interelectrode pair voltage-current regimes. The first regime, below some threshold voltage, corresponds to a high impedance gap with an almost linear relationship between interelectrode voltage and axial leakage current. The second regime, above the threshold voltage, corresponds to a low impedance gap with an almost linear relation between interelectrode voltage and axial arcing current. Based on the experiments performed it appears that the fault, or maximum power points lies between those two regimes and it is a transitory state.

2. Interelectrode arcs are rather unsteady and are present for durations of milliseconds or less. Evidence of this behavior was found in both the applied field experiment and the loading fault experiments. Ballasting, such as an external resistor in the applied field circuit or electrode boundary layers and Faraday loads, causes the interelectrode voltage drop which immediately extinguish interelectrode arcs and limit the arc current.

3. Discrepancies in threshold arcing voltage levels between the applied field tests, the loading fault experiments, and the diagonal connection experiment indicate that the arcing/arc extinguishing process may be occurring at higher frequency than standard transducers and strip chart recorders can detect. For example, under applied field conditions arcing occurred, in some cases, at 70V. Under actual MHD conditions, interelectrode arcing was not detected until a potential of 95V was achieved. The differences in equivalent ballasting and inductance between the circuits are likely to cause the variations in arc lifetime.

4. Anode wall interelectrode arcs are driven into the wall under the action of $\vec{J}\times\vec{B}$ forces. This is verified by both applied field and power generating experiments. Interelectrode insulators are cut by arcs, copper electrodes are scored by the arcs, and the G-10 fiberglass backboard and electrode tie rods are charred and become electrically conductive by interelectrode arc assault. Electrode shorting resulted only when the backboard became significantly charred. Preliminary investigations suggest this problem will be eliminated by replacing the G-10 fiberglass backboard with noncharring G-7 material. No damage to the cathode wall or sidewalls was observed in any of the experiments.

5. The fault power scales with the number of shorted electrodes. This means that if electrothermal stresses are sufficient to cause the shorting of one anode electrode pair, the time required to short successive upstream electrodes decreases resulting in a self propagating fault. However, as noted above, the electrode shorting takes place through the charred G-10 backboard material. Therefore, it is expected that alternative backboard material (G-7) will alleviate the self propagating tendency of anode axial faults.

Future work will include studies on short circuited Faraday loads, elevation of breakdown limits, fault diagnostics and fault countermeasures such as arc stretching and quenching in the interelectrode space.

References

1. Mattsson, Arne, C.J., et al., "Performance of a Self-Excited MHD Generator." Research Report 238, presented at the International Conference on Energetics, Rochester, NY, August 1965.

2. AERL, MHD Generator Component Development, Quarterly Report for July-September, 1978, FE-2519-7, UC-90g, Contract No. EF-77-C-01-2519.

3. Unkel, W. C., "Axial Field Limitations in MHD Generators," Ph.D. Thesis, Stanford University, April 1978.

4. Zalkind, V. I., et al., "Experimental Investigations of Interelectrode Breakdown in MHD Channels." Proceedings of the Seventh International Conference on MHD Electrical Power Generation, June 1980.

5. Solbes, A. and Lowenstein, A., "Electrical Non-Uniformities and Their Control in Linear MHD Channels." Proceedings of the 15th Symposium on Engineering Aspects of Magnetohydrodynamics, The University of Pennsylvania, Philadelphia, PA, May 1976.

6. Hruby, V. J., "Experimental Investigations of the Effects of Electrode Wall Temperature on MHD Channel Performance and Cathode Nonuniformities." Seventh International Conference on MHD Electrical Power Generation, June 1980.

7. Curtis, et al., "Electricity from MHD, 1968." Proceedings from Symposium on Magnetohydrodynamic Electrical Power Generation, International Atomic Energy Agency, Warsaw, July 1968.

8. AERL, MHD Generator Development, Quarterly Report for April-June 1980, FE-15615-3, UC-90g, Contract No. DE-AC010-80-ET15614.

9. AERL, MHD Generator Development, Quarterly Report for July-September 1980, FE-15614-3 UC-90g, Contract No. DE-AC010-80-ET15614.

Table 1. Fault Power Experiment Operating Conditions

Operating Parameter	Clean Wall	Slagging Wall
Mass flow	1.8 kg/sec	1.8 kg/sec
Combustor pressure	3.1 kg/cm^2	3.1 kg/cm^2
Nitrogen/oxygen	0.8	0.8
Fuel stoichiometry	10% fuel rich	10% fuel rich
Seed	K_2CO_3	K_2CO_3
Potassium concentration	1%	1%
Ash injection	0	25% carryover
Inlet Mach No.	1.5	1.5
Mid-channel magnetic field	2.33 Tesla	2.33 Tesla
Average generated power	38 kW	60 kW

Table 2. Applied Field Experiment Operating Conditions

Operating Condition	Mass Flow (kg/sec)	Combustor Press (kg/cm^2)	Nitrogen/ Oxygen	Fuel Stoichiometry	Potassium Concen. (%K)	Ash Inj. (% Carry-over)	Mid-Channel Magnetic Field (Tesla)
No. 1	0	-	-	-	0	0	0
No. 2	Air only	-	-	-	0	0	0
No. 3	1.8	3.1	0.8	Stoichiometric	0	0	0
No. 4	1.8	3.1	0.8	"	1	0	0
No. 5	1.8	3.1	0.8	"	1	25	0
No. 6	1.8	3.1	0.8	"	0	0	2.33

Table 3. Electrode Pair Test Program

Anode Electrode Pair No.	Operating Condition No.	Electrode Material	Ballast Resistance (Ω)
13-14	1	Copper	8.5
4-5	2	Molybdenum	8.5
25-26	3	Tungsten/copper	8.5
32-33	3	Tungsten/copper	8.5
10-11	3	Steel	8.5
8-9	4	Steel	8.5 and 3.8
29-30	4	Tungsten/copper	3.8
54-55	4	Steel	3.8
17-18	4	Tungsten/copper	3.8
18-19	4	Tungsten/copper	3.8
11-12	4	Steel	3.8
12-13	4	Steel	3.8
3-4	5	Molybdenum	3.8
35-36	5	Stainless Steel 26-1	3.8
52-53	5	Steel	3.8
23-24	5	Tungsten/copper	3.8
15-16	6	Nickel plated copper	8.5
33-34	6	Nickel plated copper	8.5
43-44	6	Nickel plated copper	8.5

TABLE 4
PARAMETERS CHARACTERIZING FAULT PROPAGATION

ELECTRODE PAIR	ARCING POTENTIAL (VOLTS)	DOWNSTREAM ELECTRODE TRANSVERSE PLASMA CURRENT (AMPS)	MAGNETIC FIELD (TESLA)	SHORTING TIME (MIN.)	INSULATOR CONDITION / BACKBOARD CONDITION
27–28	95	52	2.0	64	ARC TRACKS / CHARRED
26–27	95	56	2.0	20	ARC TRACKS / CHARRED
25–26	74	60	1.9	.6	NO DAMAGE / CHARRED
24–25	105	60	1.9	9	ARC TRACKS / CHARRED
23–24	85	62	1.8	15	ARC TRACKS / CHARRED

Table 5. Summary of Pre and Post-Breakdown Performance Parameters

	Measured Average Power (kW)	Measured Average Hall Voltage (volts)
Before Breakdown	68	670
After Breakdown	55	590
Ratio (after/before)	.8	.9

Table 6. Diagonal Connection Operating Conditions

Operating Parameter	Operating Condition No. 1	2	3	4	5
Total Mass Flow, kg/sec	1.8	1.8	1.8	1.8	1.8
Combustor Pressure, kg/cm^2	3.1	3.1	3.1	3.1	3.1
Nitrogen/Oxygen	0.8	0.8	0.8	0.8	0.6
Fuel Stoichiometry	10% fuel rich	10% fuel rich	10% fuel rich	10% fuel rich	10% fuel rich
Seed	K_2CO_3	K_2CO_3	K_2CO_3	K_2CO_3	K_2CO_3
Potassium Concentration	1%	1%	1%	1%	1%
Ash	Eastern	Eastern	Eastern	Western	Western
Ash Injection Rate (Equivalent Carryover Rate	25%	25%	25%	25%	25%
Inlet Mach No.	1.5	1.5	1.5	1.5	1.5
Magnetic Field (Mid-Channel)	2.33	2.33	2.33	2.33	2.33
Load	10Ω	6.7Ω	15Ω	15Ω	15Ω

Table 7. Fly Ash Mineral Analysis*

Mineral Analysis	Eastern Ash % Weight Ignited	Western Ash % Weight Ignited
Silica, SiO_2	42.69	45.05
Alumina, Al_2O_3	22.55	22.14
Titania, TiO_2	1.10	0.99
Ferric Oxide, Fe_2O_3	19.13	5.05
Lime, CaO	5.70	18.00
Magnesia, MgO	1.24	4.60
Potassium Oxide, K_2O	1.80	0.45
Sodium Oxide, Na_2O	1.72	0.57
Sulfur Trioxide, SO_3	3.24	1.01
Phos. Pent. P_2O_5	0.71	0.41
Undetermined	0.12	1.73
	100.00	100.00

*Analysis performed by Commercial Testing & Engineering Co., Chicago, IL

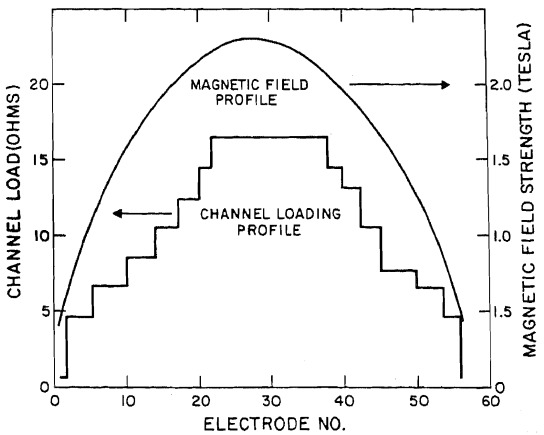

Fig. 1 Channel Loading and Magnetic Field Profiles

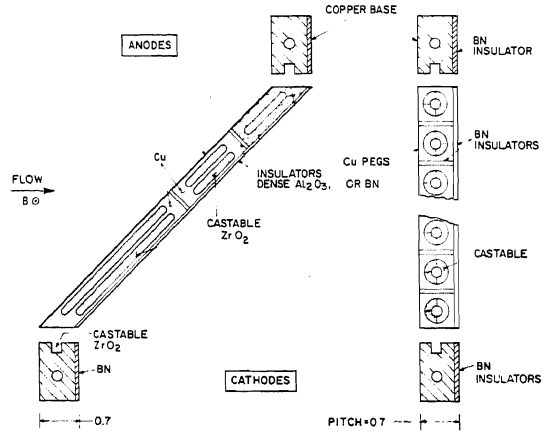

Fig. 2 Gas Exposed Surfaces of Bar and Peg Type Sidewalls

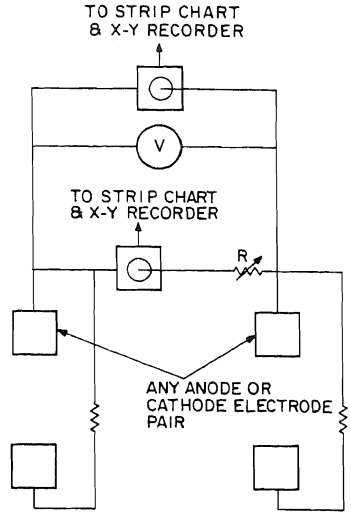

Fig. 3 Schematic of Fault Power Coupling Experiment Wiring Connections and Instrumentation

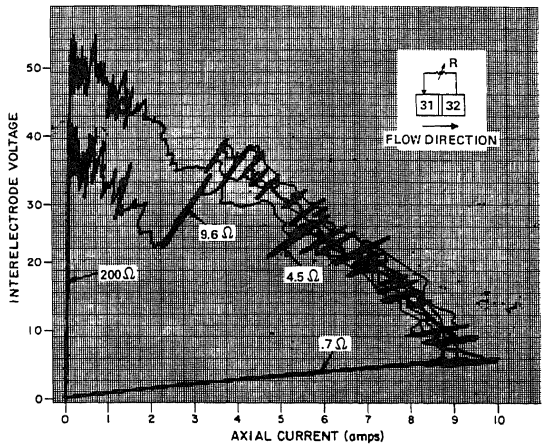

Fig. 4 Real Time Plot of Anode Pair 31-32 Voltage-Current Characteristic for Slagging Wall Power Generating Conditions

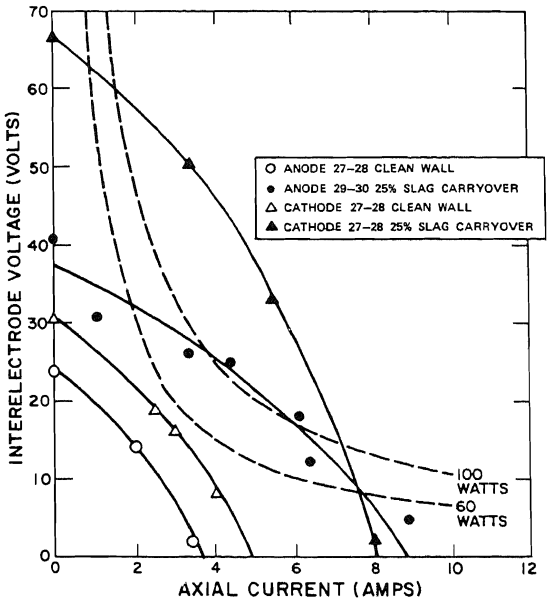

Fig. 5 Clean and Slagging Wall Anode and Cathode Voltage-Current Characteristics for Power Generating Conditions

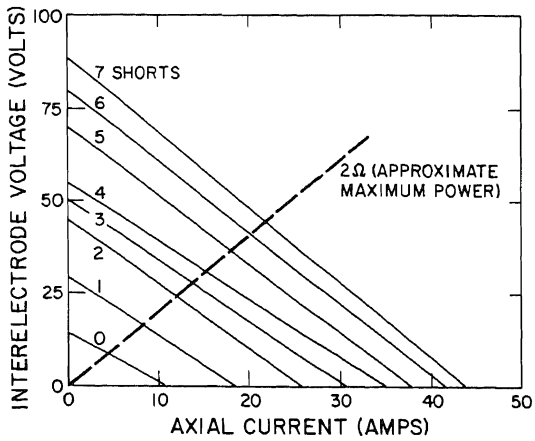

Fig. 6 Linear Approximation of Voltage-Current Characteristics as a Function of Shorted Anodes

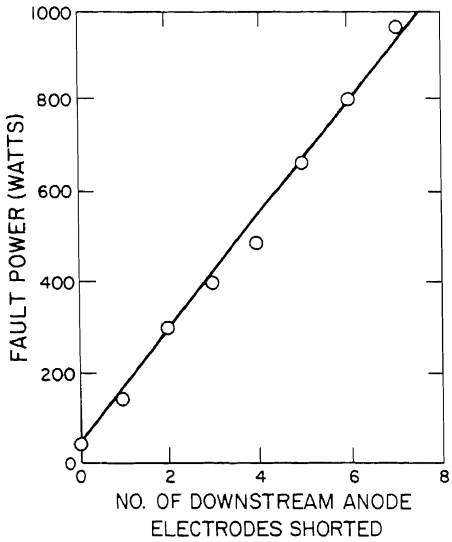

Fig. 7 Fault Power as a Function of Shorted Anodes

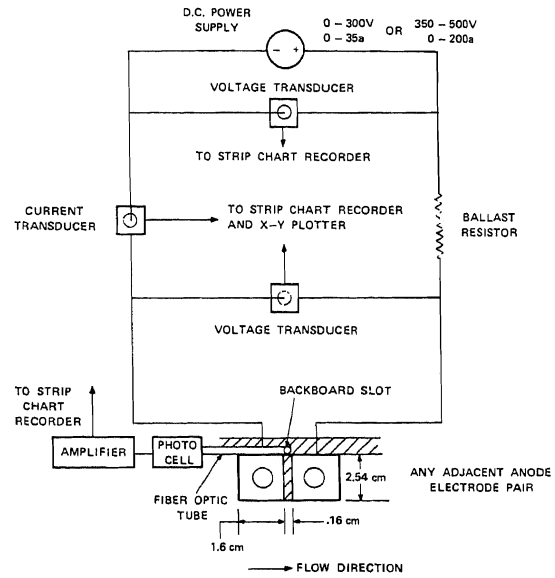

Fig. 8 Schematic of Applied Field Experiment Wiring Connections and Instrumentation

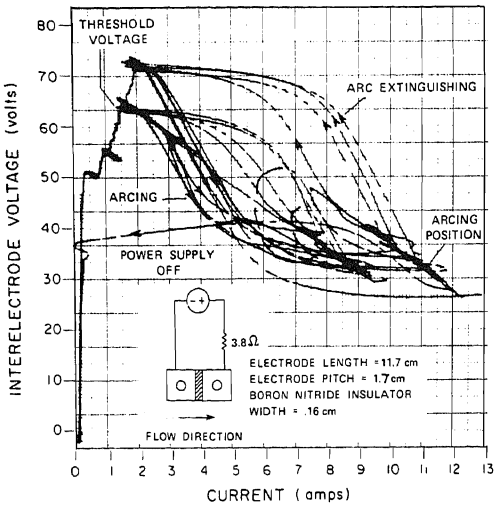

Fig. 9 Real Time Plot of Anode Pair 52-53 Voltage-Current Characteristic for Slagging Wall Applied Field Conditions

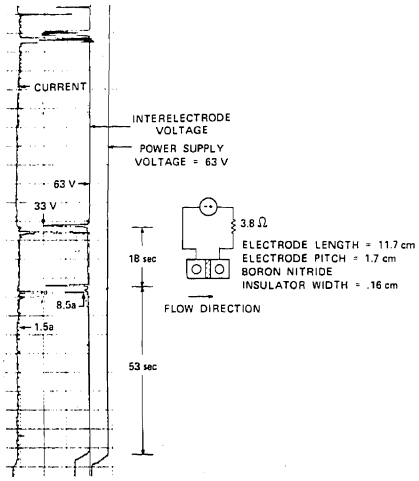

Fig. 10 Strip Chart Record of Anode Pair 52-53 for Slagging Wall Applied Field Conditions

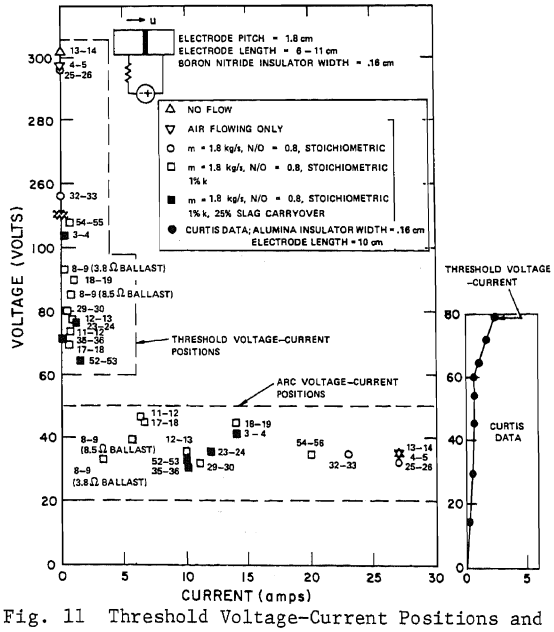

Fig. 11 Threshold Voltage–Current Positions and Arcing Voltage–Current Positions for Applied Field Tests

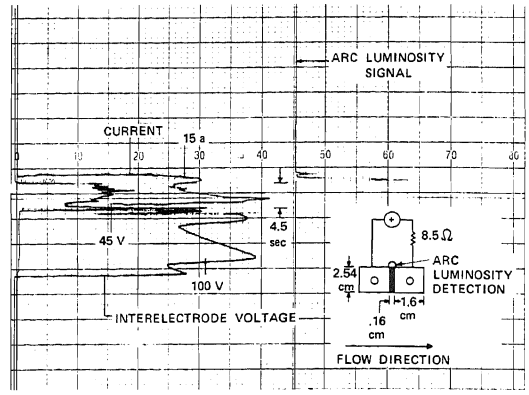

Fig. 12 Strip Chart Record of Applied Field Test in the Presence of a Magnetic Field

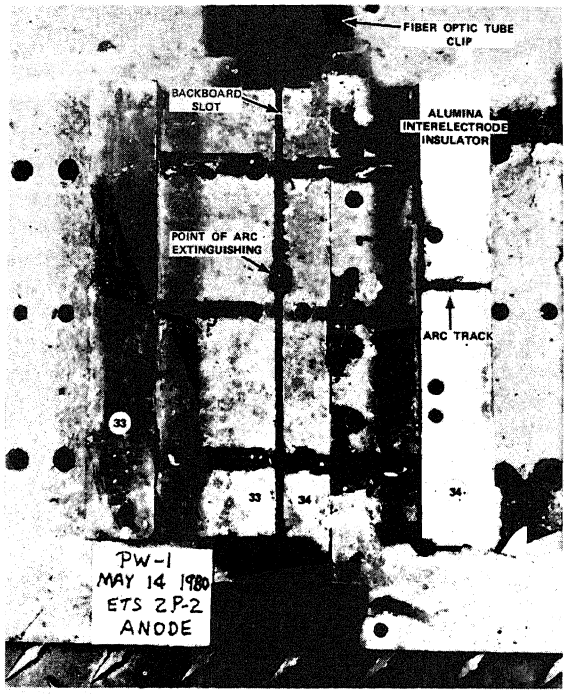

Fig. 13 Post-Test Photograph of Anode Pair 33-34 Showing Arc Damage for Applied Field Conditions in the Presence of a Magnetic Field

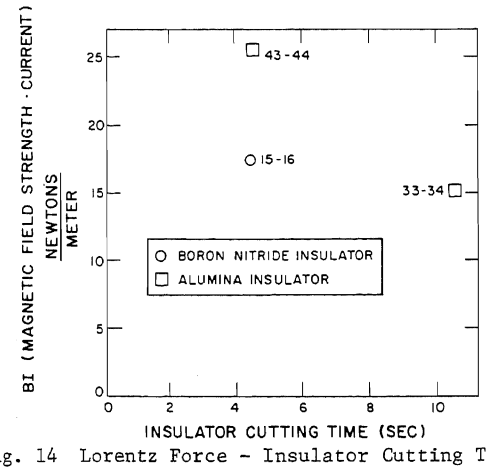

Fig. 14 Lorentz Force - Insulator Cutting Time Relationship

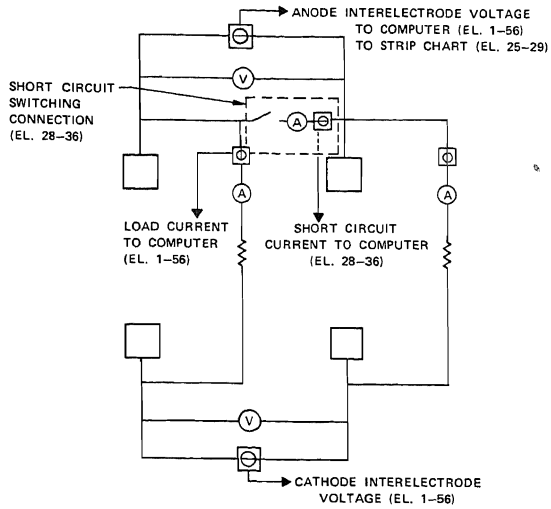

Fig. 15 Schematic of Shorted Anode Experiment
Wiring Connections and Instrumentation

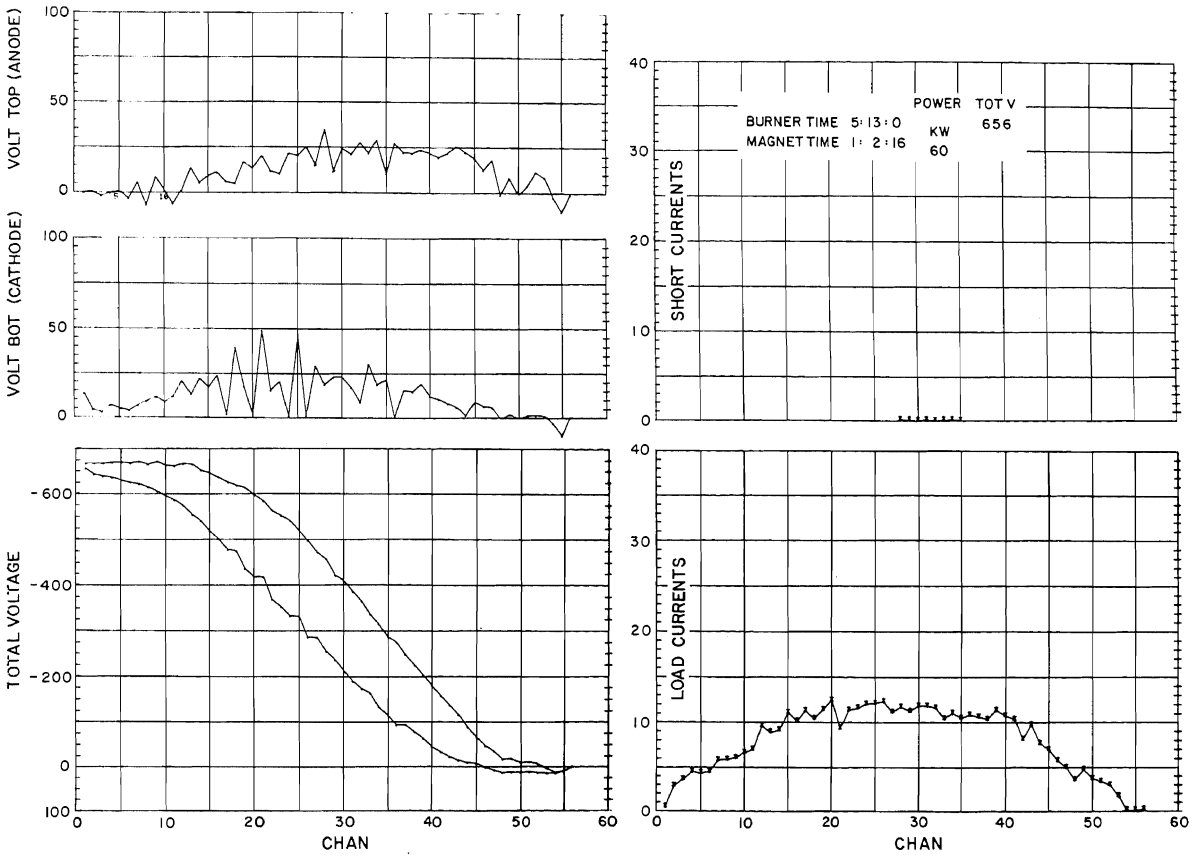

Fig. 16a Computer Record of Electrical Parameters for Typical Slagging Wall Operation

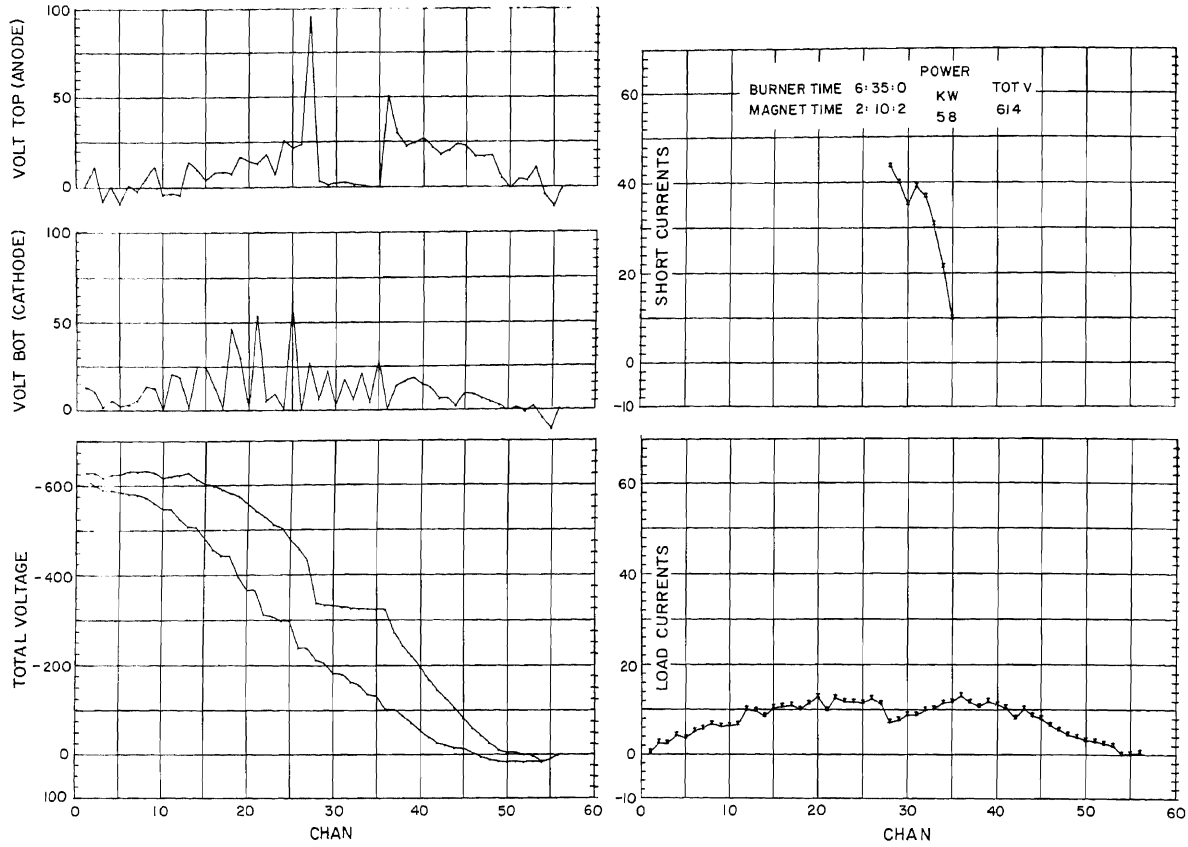

Fig. 16b Computer Record of Electrical Parameters with Anodes 28 through 36 Externally Shorted

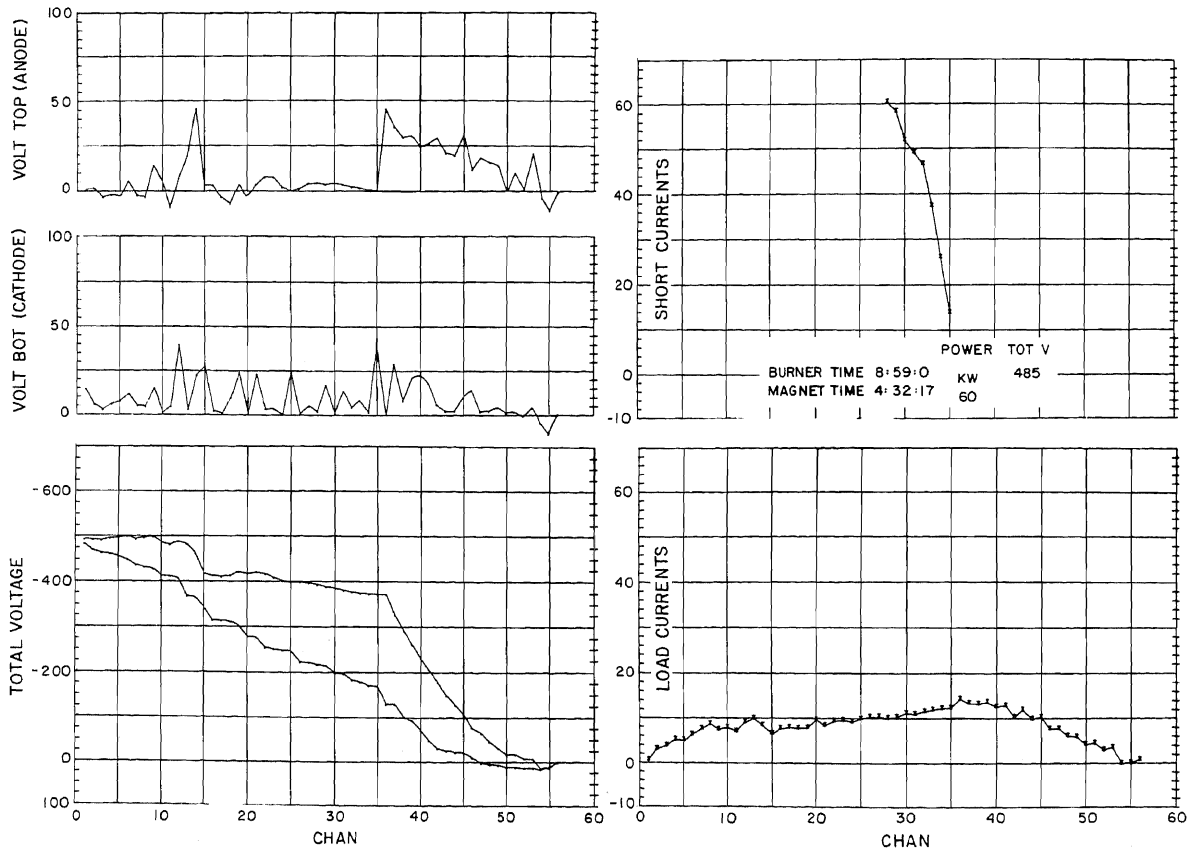

Fig. 16c Computer Record of Electrical Parameters with Arc Damaged Electrically Conductive Backboard

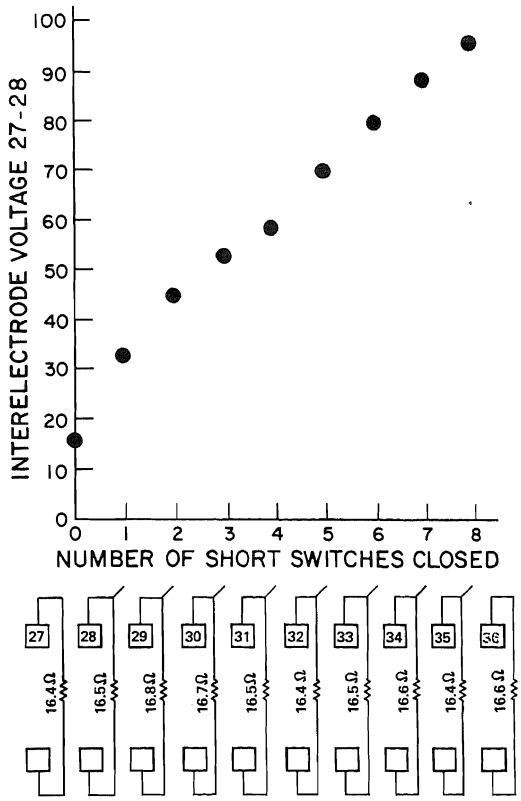

Fig. 17 Anode Pair 27-28 Interelectrode Voltage as a Function of Short Switches Closed

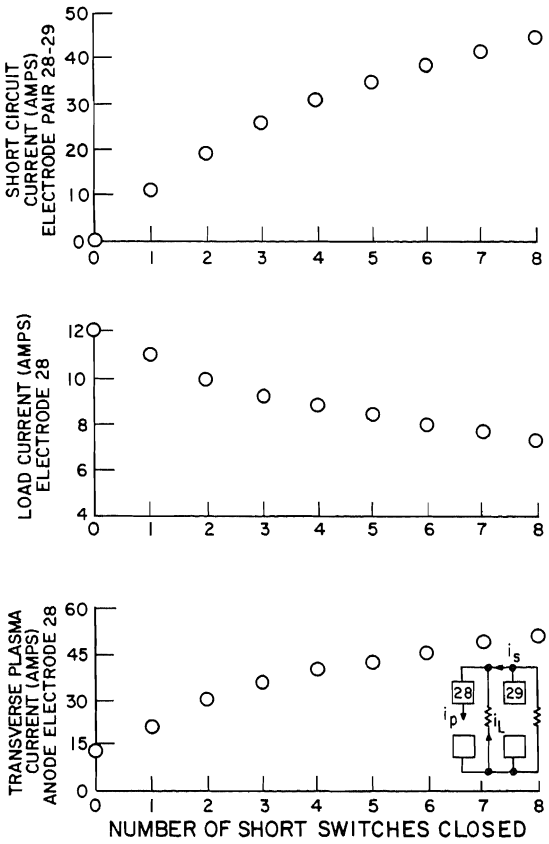

Fig. 18 Anode Pair 27-28 Short Circuit Current, Load Current 28, and Transverse Plasma Current 28 as a Function of Short Switches Closed

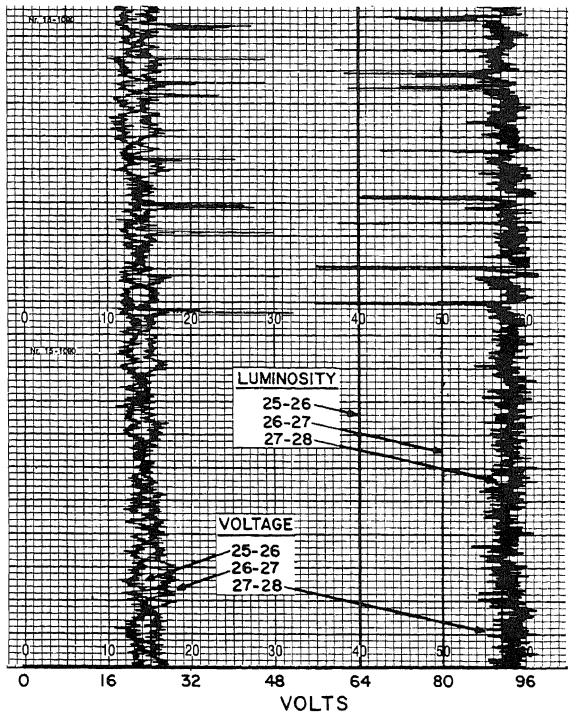

Fig. 19 Strip Chart Record with Electrodes 28-35 Externally Shorted

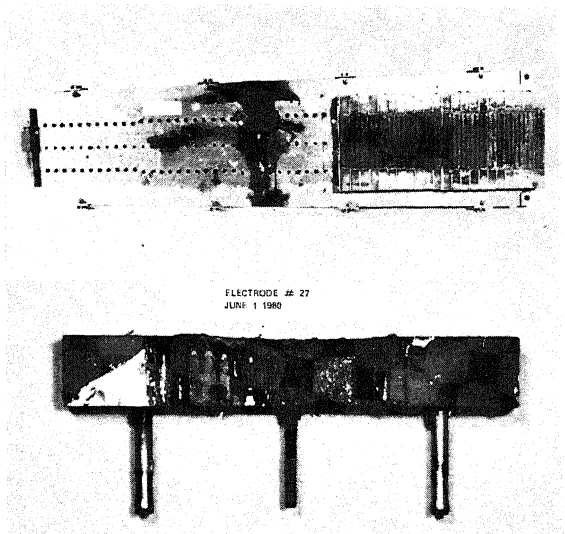

Fig. 20 Post-Test Photographs Showing Anode Wall Backboard Condition (Top) and the Upstream Surface of Anode 27 (Bottom)

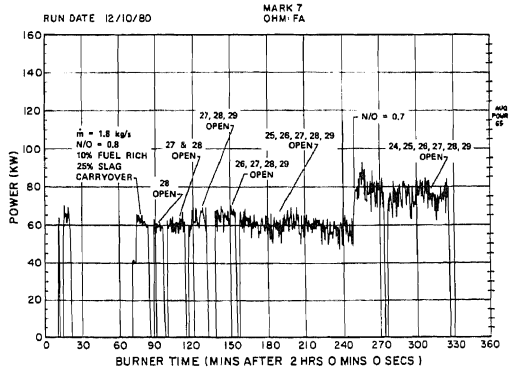

Fig. 21 Generated Power versus Burner Time for Open Faraday Load Experiment

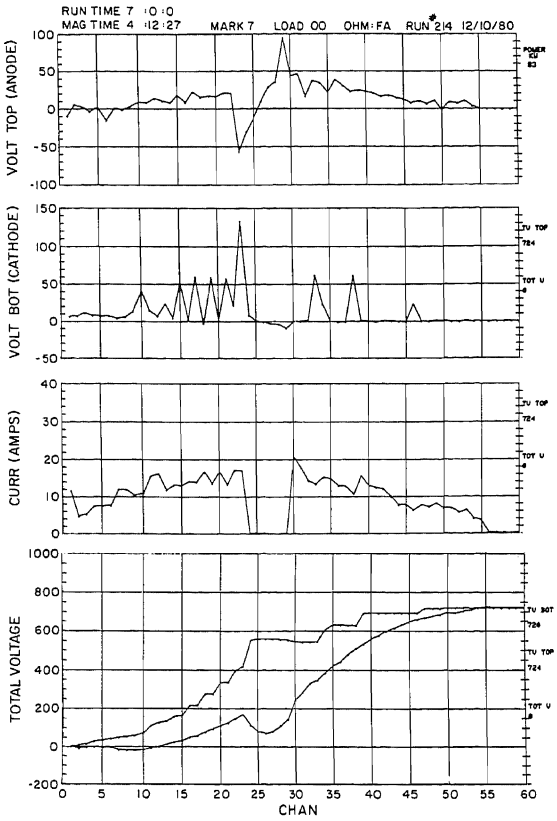

Fig. 22 Computer Record of Electrical Parameters with Loads 24 through 29 Removed

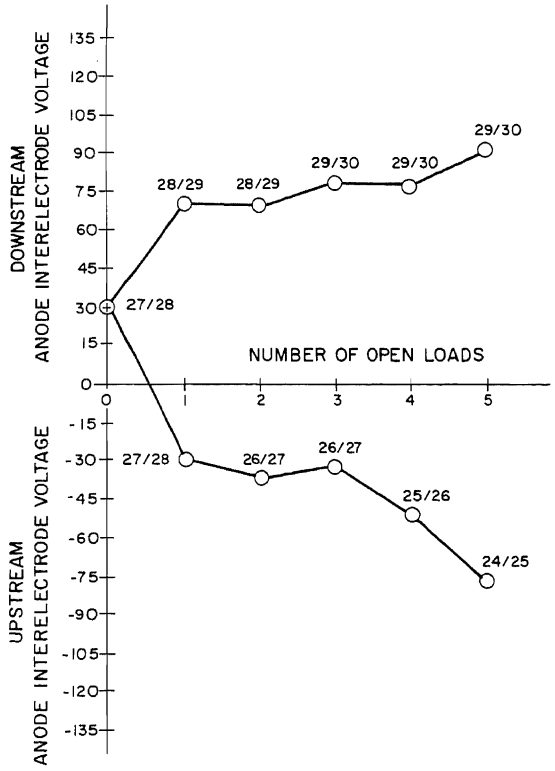

Fig. 23 Anode Interelectrode Voltages as a Function of Number of Loads Removed

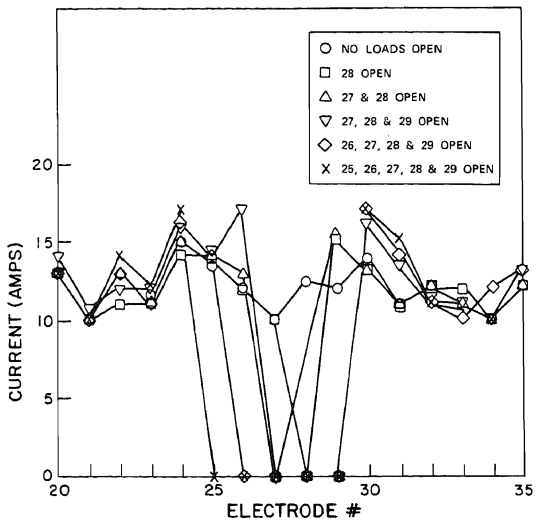

Fig. 24 Spatial Distribution of Load Currents as a Function of Loads Removed

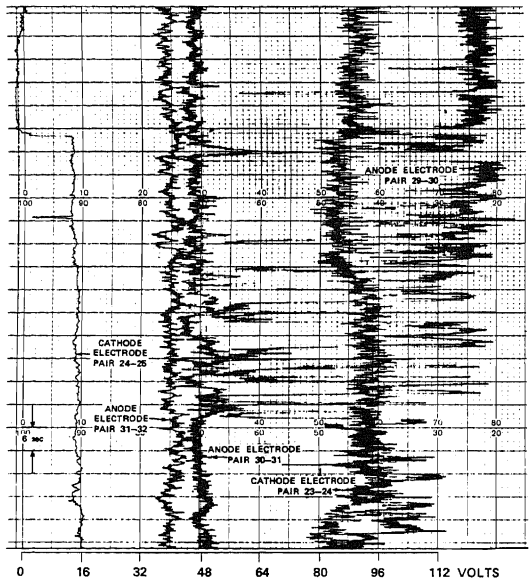

Fig. 25 Strip Chart Record with Loads 25 through 29 Removed

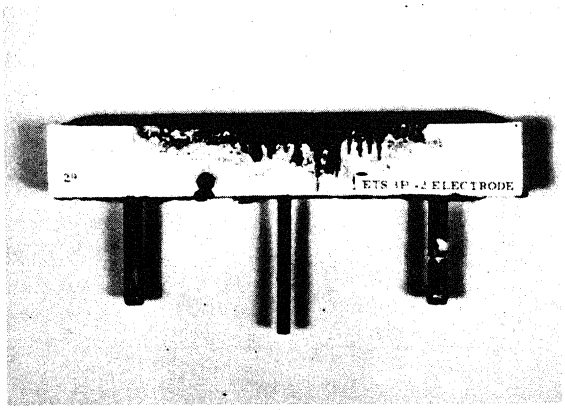

Fig. 26 Post-Test Photograph of the Upstream Surface of Anode 29

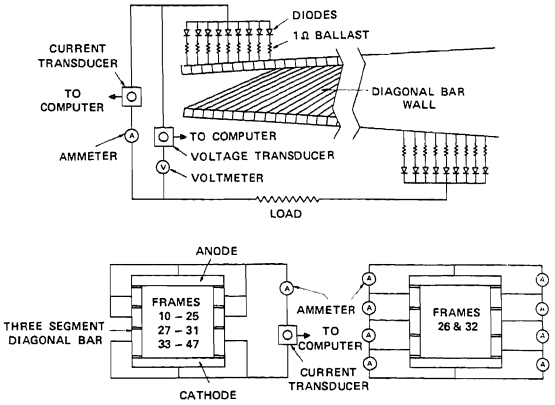

Fig. 27 Schematic of Diagonally Connected Channel Showing Wiring and Instrumentation

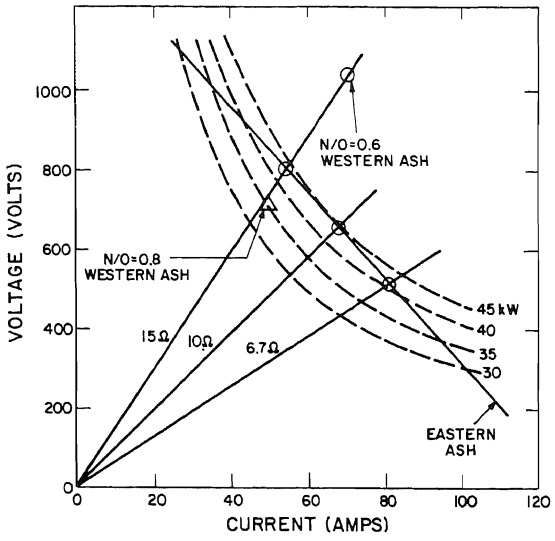

Fig. 29 Diagonally Connected Generator Load Line

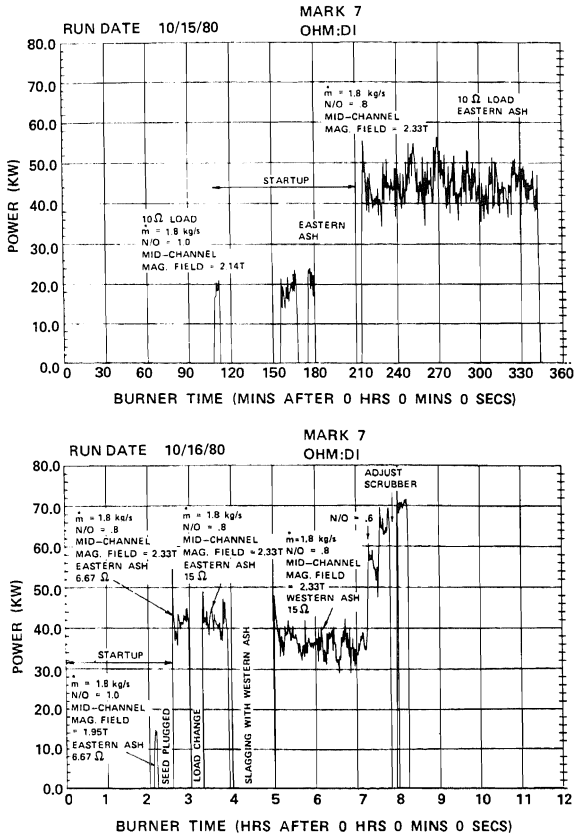

Fig. 28 Generated Power versus Burner Time for Diagonally Connected Channel Investigation

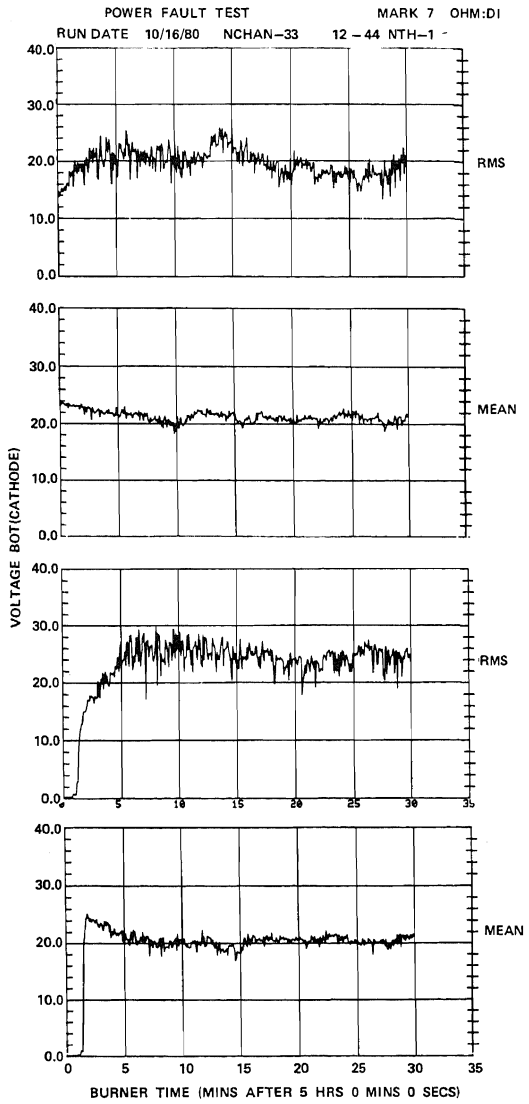

Fig. 30 RMS and Mean Cathode Voltages for Eastern Ash (Top) and Western Ash (Bottom)

WINDOW FRAME CURRENT DISTRIBUTION

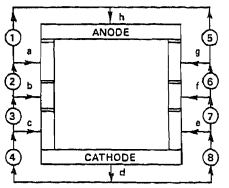

OPERATING CONDITION

$\dot{m}$ = 1.8 kg/s 1% K
N/O = 0.8 B = 2.3 T
10% FUEL RICH

BURNER TIME (min.)	AMMETER READING (amps) 1	2	3	4	5	6	7	8	BAR CURRENT (amps) a	b	c	d	e	f	g	h
FRAME 26, 10Ω LOAD																
236	0	2	2	7	10	0	0	0	2	0	–5	7	0	0	–10	10
252	3	3	3	5	3	5	5	3	0	0	–2	8	2	0	2	6
269	2	2	2	7	2	7	7	2	0	0	–5	9	5	0	5	4
282	2	2	2	10	2	5	5	3	0	0	–8	13	2	0	3	4
299	2	5	6	7	5	6	6	3	3	1	–1	10	3	0	1	7
330	2	4	5	6	5	3	3	2	2	1	–1	8	1	0	–2	7
349	3	5	6	5	3	4	4	2	2	1	1	7	2	0	1	6
FRAME 32, 10Ω LOAD																
236	5	5	5	5	–5	7	7	2	0	0	0	7	5	0	12	0
252	0	1	0	1	3	0	0	0	1	–1	–1	1	0	0	–3	3
269	9	10	10	11	–10	11	11	11	1	0	–1	22	0	0	21	–1
282	2	10	10	10	–5	11	11	5	8	0	0	15	6	0	16	–3
299	2	8	9	9	–4	10	10	5	6	1	0	14	5	0	14	–2
330	2	3	3	–11	10	0	0	0	1	0	14	–11	0	0	–10	12
349	2	3	3	–5	–3	2	2	1	1	0	8	–4	1	0	5	–1

Fig. 31 Data from Completely Instrumented Diagonal Frames

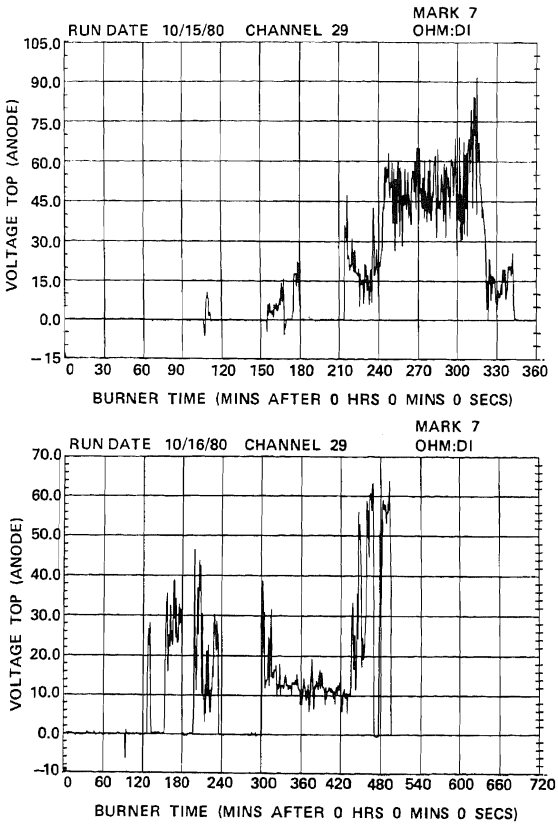

Fig. 32 Anode Pair 29-30 Interelectrode Voltage as a Function of Burner Time

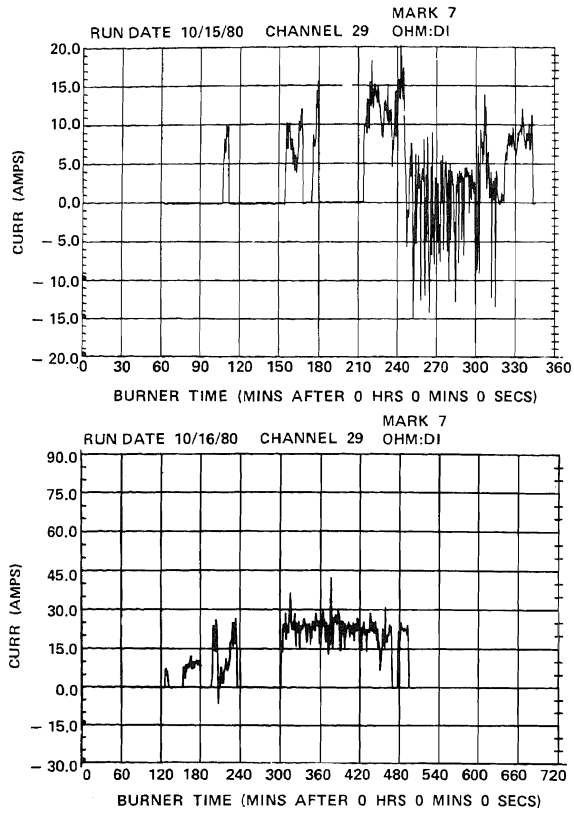

Fig. 33 Frame 29 Total Current as a Function of Burner Time

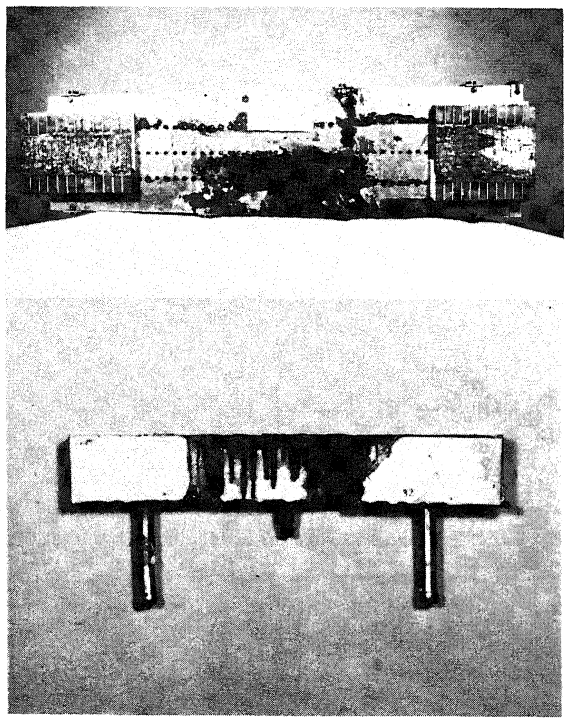

Fig. 34 Post-Test Photographs Showing Anode Wall Backboard Condition (Top) and the Upstream Surface of Anode 32 (Bottom)